LA-UR- 08-7265

Approved for public release; distribution is unlimited.

Title: A large area polarized 3He neutron spin filter

Author(s): T.E. Chupp, K.P. Coulter, M. Kandes, M. Sharma, T.B. Smith, G. Jones, W.C. Chen, T.R. Gentile, D.R. Rich, B. Lauss, M.T. Gericke, R.C. Gillis, S.A. Page, J.D. Bowman, S.I. Penttila, W.S. Wilburn, M. Dabaghyan, F.W. Hersman, and M. Mason

Intended for: Nuclear Instruments and Methods in Physics A

Los Alamos
NATIONAL LABORATORY
EST. 1943

Los Alamos National Laboratory, an affirmative action/equal opportunity employer, is operated by the Los Alamos National Security, LLC for the National Nuclear Security Administration of the U.S. Department of Energy under contract DE-AC52-06NA25396. By acceptance of this article, the publisher recognizes that the U.S. Government retains a nonexclusive, royalty-free license to publish or reproduce the published form of this contribution, or to allow others to do so, for U.S. Government purposes. Los Alamos National Laboratory requests that the publisher identify this article as work performed under the auspices of the U.S. Department of Energy. Los Alamos National Laboratory strongly supports academic freedom and a researcher's right to publish; as an institution, however, the Laboratory does not endorse the viewpoint of a publication or guarantee its technical correctness.

Form 836 (7/06)

Available online at www.sciencedirect.com
ScienceDirect
ELSEVIER
Nuclear Instruments and Methods in Physics Research A 574 (2007) 500–509
NUCLEAR INSTRUMENTS & METHODS IN PHYSICS RESEARCH Section A
www.elsevier.com/locate/nima

A large area polarized ^{3}He neutron spin filter

T.E. Chupp[a,*], K.P. Coulter[a], M. Kandes[a], M. Sharma[a], T.B. Smith[b], G. Jones[c], W.C. Chen[d], T.R. Gentile[d], D.R. Rich[d], B. Lauss[e], M.T. Gericke[f,g], R.C. Gillis[f], S.A. Page[f], J.D. Bowman[h], S.I. Penttila[h], W.S. Wilburn[h], M. Dabaghyan[i], F.W. Hersman[i], M. Mason[i]

[a]*Focus Center, University of Michigan, Ann Arbor, MI 48104, USA*
[b]*University of Dayton, Dayton, OH 45469, USA*
[c]*Hamilton College, Hamilton, NY 13323, USA*
[d]*NIST, Gaithersburg, MD 20899, USA*
[e]*University of California, Berkeley, CA 94720, USA*
[f]*University of Manitoba, Winnipeg, Man., Canada R3T 2N2*
[g]*Thomas Jefferson National Accelerator Facility, Newport News, VA 23606, USA*
[h]*Los Alamos National Lab, Los Alamos, NM 85777, USA*
[i]*University of New Hampshire, Durham, NH 03824, USA*

Received 19 July 2006; received in revised form 24 January 2007; accepted 13 February 2007
Available online 2 March 2007

Abstract

A large area polarized ^{3}He neutron spin filter has been developed and tested in long-term operation. The polarizer cells have area $50\,\mathrm{cm}^2$ and larger allowing access to a large area neutron beam. Polarization of ^{3}He up to $57 \pm 1\%$ was measured by monitoring the neutron transmission through the ^{3}He. The polarization was maintained over the course of several weeks, but the maximum attainable polarization declined over the course of a year-long run as the cell degraded, possibly due to long-term exposure to the neutron beam at high temperatures. The resulting neutron polarization and transmission are velocity dependent and are optimized for 5 Å. Cell construction, polarizer design, performance, and polarimetry are described in this paper.
© 2007 Published by Elsevier B.V.

Keywords: Polarized neutrons; Pulsed neutrons; Symmetry tests; Spin filters; Polarized ^{3}He

1. Introduction and motivation

Polarized neutron beams are sought for a wide variety of applications including neutron scattering [1], neutron beta decay [2], and hadronic parity violation [3]. For beta decay and parity violation experiments, which are in part statistics limited, the largest practical cross-sectional area and long-term operation are essential. For the next generation of polarized neutron beta decay experiments that follow PERKEO-2 [4], precise knowledge of the neutron polarization at the 10^{-3}–10^{-4} level is essential to reducing systematic effects. With the completion of the Spallation Neutron Source, new opportunities will emerge to exploit the neutron time-of-flight dependence of polarization observables [5]. Polarized ^{3}He has long been recognized for its potential as a neutron polarizer due to the nearly perfect spin dependence of the absorption cross-section for the ^{3}He(n,p)^{3}H reaction. Techniques for producing sufficient quantities and polarization of ^{3}He have steadily improved for both spin-exchange polarization [6,7] and metastability exchange [1,8]. A spin-exchange pumped ^{3}He spin filter can be exceptionally useful in these applications because of the large area, continuous polarization, low gamma backgrounds, modest (e.g. 1 mT) magnetic fields, and the ease of reversing the ^{3}He spin with NMR techniques.

The ^{3}He spin filter described in this paper was developed for the $\vec{n} + p \rightarrow d + \gamma$ experiment. The goal of the experiment is the measurement of the parity violating asymmetry A_γ, i.e. the correlation of γ-ray emission with respect to the neutron spin, that arises due to the weak

*Corresponding author.
E-mail address: chupp@umich.edu (T.E. Chupp).

0168-9002/$ - see front matter © 2007 Published by Elsevier B.V.
doi:10.1016/j.nima.2007.02.091

interaction effects in the $^1H(n,\gamma)^2H$ reaction. The weak interaction, solidly established as part of the Standard Model, is generally well characterized at the quark level. An exception is the flavor-conserving, non-leptonic sector, which is addressed by nucleon–nucleon parity violation measurements. The full strong interaction (i.e. QCD) description of nuclear forces must include the hadronic weak interaction, and a variety of few nucleon measurements aim to complete the description [9]. The observable A_γ isolates the $\Delta I = 1$ component of the nucleon–nucleon weak interaction, and thus the measurement of A_γ can accurately reveal the strength of the pion contribution and considerably reduce the statistical and theoretical uncertainty in the value of the hadronic weak coupling constant f_π.

A ^{3}He spin filter can also be crucial to measurement of correlations in polarized neutron beta-decay. Measurements of parity [4] and time reversal violation [2,10] probe the Standard Model couplings and physics beyond the Standard Model. The strength of parity violation in the asymmetry of electron emission with respect to the neutron spin (the A-coefficient) has been measured with precision better than 1% [4], but the systematic error due to the uncertainty on the neutron polarization has become a major limitation. The goal of the next generation of these experiments is 0.1% or better [4,11,12], thus the ability to reverse the spin-filter polarization sense with respect to the neutron-spin transport magnetic fields and the precisely known time-of-flight dependence of the neutron polarization is a valuable tool. Our analysis of the $\vec{n} + p \rightarrow d + \gamma$ spin filter performance illustrates the feasibility and the challenges of 0.1% and better polarimetry for a pulsed cold neutron beam.

2. Apparatus and techniques

The neutron spin filter is a key component of the $\vec{n} + p \rightarrow d + \gamma$ experiment at LANSCE, the Los Alamos Neutron Science Center. In Fig. 1, a schematic of the $\vec{n} + p \rightarrow d + \gamma$ experiment on FP12 [13], is provided for orientation. The pulsed neutron beam is provided by spallation produced by 800 MeV protons incident on a tungsten target at 20 Hz. The neutrons thermalize in a 20 K cold hydrogen moderator [14] viewed by a super-mirror neutron guide [15]. A chopper defines a specified wavelength range and cuts off longer wavelength neutrons from each pulse, preventing them from traversing the apparatus during the next pulse.

The entire experiment is enclosed within a shielding cave constructed of steel and borated plastic. The steel also serves as a flux return for the magnetic field. A uniform vertical magnetic field of about 1 mT is maintained by a set of coils. The neutrons are polarized by the ^{3}He spin filter and pass through an RF spin flipper before interacting with the liquid para-hydrogen target. The nominal neutron polarization is in the vertical direction. The 2.2 MeV γ-rays from neutron capture in the 16 l hydrogen target will be detected by an array of 48 CsI gamma detectors. The γ-ray angular distribution is $A_\gamma \cos\theta$, where θ is the angle between the neutron spin and the photon momentum. Because of the high neutron rates, the detectors and monitors are operated in current mode by converting the scintillation light from CsI(Tl) crystals to charge using vacuum photodiodes [16]. The photocurrents are then converted to voltages and amplified by low-noise solid-state electronics [17]. The neutron beam is monitored by three monitors, labeled M1, M2, and M3. These measure the neutron flux at each position. The monitors M1 and M2 are thin, each transmitting about 94% of the neutron beam (at 5 Å). The monitor M3 is thick, but data from M3 are not used for the analysis presented here. The effect of the ^{3}He on the neutron flux is used to determine the neutron and ^{3}He polarizations as described below.

2.1. Spin filter principles

The primary ^{3}He-neutron interaction is absorption through a broad unbound 0^+ resonance in $^3He + n$, which breaks up into ^{1}H and ^{3}H [18]. Resonance absorption occurs only if the neutron and ^{3}He spin are in a singlet state, i.e. the neutron and ^{3}He spins are *opposite*. Thus, the absorption cross-section is nearly completely spin dependent and proportional to neutron wavelength λ. For neutron spin up (↑) or down (↓) with respect to the ^{3}He

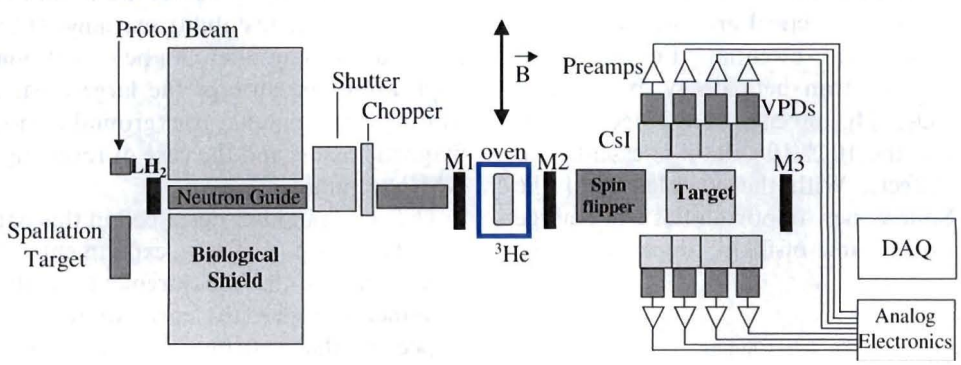

Fig. 1. Schematic of the layout of the $\vec{n} + p \rightarrow d + \gamma$ experiment at LANSCE Flight Path 12. The apparatus is inside a cave lined with soft iron that serves as magnetic shielding and a flux return. The magnetic field is vertical (up or down).

spin, the cross-sections are given by

$$\sigma^{\uparrow} = \sigma_0 \frac{\lambda}{\lambda_0} \frac{1 - P_3}{2}, \quad \sigma^{\downarrow} = \sigma_0 \frac{\lambda}{\lambda_0} \frac{1 + P_3}{2} \tag{1}$$

where $\sigma_0 = 5333\,\mathrm{b}$ is the thermal cross-section at $\lambda_0 = 1.8\,\text{Å}$ and $v_0 = 2200\,\mathrm{m/s}$ [19], and P_3 is the ^{3}He polarization. In addition to absorption, neutrons are scattered by ^{3}He in both the singlet and triplet states with a 3.1 b cross-section [19]. For N_0 unpolarized neutrons incident on polarized ^{3}He, the transmitted neutron beam will have unequal fractions of spin-up and spin-down neutrons given by

$$N^{\uparrow} = \frac{N_0}{2} \exp\left(-\sigma_0 t_3 \frac{\lambda}{\lambda_0}[1 - P_3]\right),$$
$$N^{\downarrow} = \frac{N_0}{2} \exp\left(-\sigma_0 t_3 \frac{\lambda}{\lambda_0}[1 + P_3]\right) \tag{2}$$

where t_3 is the ^{3}He areal density. For a perfect system, the neutron polarization is

$$P = \frac{N^{\uparrow} - N^{\downarrow}}{N^{\uparrow} + N^{\downarrow}} = \tanh\left(\sigma_0 t_3 P_3 \frac{\lambda}{\lambda_0}\right) \tag{3}$$

and the transmission is

$$T = \frac{N^{\uparrow} + N^{\downarrow}}{N_0} = \exp\left(-\sigma_0 t_3 \frac{\lambda}{\lambda_0}\right) \cosh\left(\sigma_0 t_3 P_3 \frac{\lambda}{\lambda_0}\right). \tag{4}$$

These relationships are used in the analysis using the monitors M1 and M2, described in Section 3. The neutron polarization can be made arbitrarily close to unity by increasing t_3 for any finite P_3; however, the transmission is reduced as t_3 increases for any P_3 less than unity. Polarization of ^{3}He greater than 50% is routine, and the figure of merit, the appropriately averaged $\langle P^2 T \rangle$ can be optimized for a specified wavelength range and P_3.

2.2. ^{3}He polarization

The ^{3}He is polarized via spin exchange with laser polarized rubidium [6,20,21]. Spin exchange has been applied broadly for neutron spin filters [7,22,23], polarized targets for electron scattering [24–26], for medical imaging [27], and has been extensively studied [28–30], though a complete understanding of the limitations of spin exchange has not yet been compiled [30]. The principle has been described in detail in many earlier papers (see for example Ref. [21,28,29,31]), and is described only briefly here.

Most generally the polarization of an ensemble of ^{3}He nuclei with $P_3(0) = 0$ can be written as

$$P_3(t) = \frac{\langle P_{\mathrm{Rb}} n_{\mathrm{Rb}} \rangle k_{\mathrm{SE}}}{\gamma_{\mathrm{SE}} + \Gamma_3}(1 - \mathrm{e}^{-(\gamma_{\mathrm{SE}} + \Gamma_3)t}). \tag{5}$$

Where

$$\langle P_{\mathrm{Rb}} n_{\mathrm{Rb}} \rangle = \int_{\mathrm{cell}} \frac{n_{\mathrm{Rb}}(\vec{r}) \gamma_{\mathrm{opt}}(\vec{r})}{\gamma_{\mathrm{opt}}(\vec{r}) + \Gamma_{\mathrm{SD}}(\vec{r})} \mathrm{d}^3 r. \tag{6}$$

Here, $n_{\mathrm{Rb}}(\vec{r})$ is the rubidium number density, and $\gamma_{\mathrm{opt}}(\vec{r})$ is the position dependent convolution of the laser intensity and photon absorption cross-section. The spin-destruction rate per rubidium atom, $\Gamma_{\mathrm{SD}}(\vec{r})$, is dominated by bulk Rb–Rb collisions with additional contributions from Rb–^{3}He, and Rb–N_2 collisions. Spin destruction is stronger closer to the cell walls due to diffusion [32]. The velocity averaged spin-exchange rate is $\gamma_{\mathrm{SE}} = k_{\mathrm{SE}} \langle n_{\mathrm{Rb}} \rangle$ with $k_{\mathrm{SE}} = \langle \sigma_{\mathrm{SE}} v \rangle$, and Γ_3 is the intrinsic cell relaxation rate due to the combined contributions of dipole–dipole relaxation [33], wall relaxation [34], relaxation from diffusion through magnetic field gradients [35], and other mechanisms [30]. The wall relaxation rate is affected by paramagnetic impurities, such as iron atoms, and the glass permeability [36]. A fundamental limit on Γ_3 is the ^{3}He dipole–dipole relaxation rate, given by $\Gamma_{\mathrm{d}} \approx 0.0013\,(n_3/n_0)\,\mathrm{h}^{-1}$, where n_3 is the ^{3}He number density and $n_0 = 2.68 \times 10^{19}\,\mathrm{cm}^{-3}$ is the n_3 at STP [33]. The factor Γ_3 may also include possible temperature or rubidium density dependent contributions to cell relaxation [30,37]. Diffusion in magnetic field gradients increases as the pressure decreases. The largest component of the magnetic field gradient across the spin filter cell was measured to be $60 \pm 30\,\mu\mathrm{T/m}$, and ^{3}He relaxation rates less than $1/(150\,\mathrm{h})$ were measured, indicating that the relevant magnetic field gradients were sufficiently small. In contrast to electron-scattering targets, which operate at three to 10 times higher ^{3}He pressures, large area neutron spin filter cells are limited to about atmospheric pressure for mechanical reasons. Thus, neutron spin filters have lower dipole–dipole contribution to Γ_3. With a sufficiently uniform magnetic field, γ_{SE} can be varied (by varying the cell temperature and thus n_{Rb}) to maximize the ^{3}He polarization. Note, however, that cell temperature is a complicated variable, which affects wall relaxation, diffusion, the rubidium polarization gradient at the wall [28], Rb–Rb collisions [28], and absorption of the broadband laser light [38]. In general, the single cell neutron spin filter runs at lower temperature and lower laser intensity than electron scattering targets but absorbs less of the broadband laser light. (The absorption linewidth for ^{3}He is $\gamma = 18 n/n_0\,\mathrm{GHz}$.) Electron scattering targets typically operate above 170 °C with optical pumping time constants of a 10–14 h and a laser power density of $2\,\mathrm{W/cm}^2$. For the spin filter running at 160 °C, the time constant was about 20 h and laser intensity $0.4\,\mathrm{W/cm}^2$.

2.3. Spin filter cells

Table 1 lists an inventory of spin filter cells constructed for the $\vec{n} + p \rightarrow d + \gamma$ experiment. The cells are large and roughly cylindrical with inside diameter about 10 cm or greater and length about 5 cm. The cells are made of GE-180 [39] boron free alumino-silicate glass. The neutron transmission through 3.5 mm of GE180 glass, over the range important for the $\vec{n} + p \rightarrow d + \gamma$ experiment, is shown in Fig. 2. The wavelength dependence is relatively flat and $\approx 94\%$. The cells are blown from glass melted from 15 mm stock tubing. A detailed description of cell production is presented in [40]. In short, a single cell is

Table 1
Cells made at NIST for the $n + p \rightarrow d + \gamma$ experiment

Cell name	Diameter (cm)	Volume (cm^3)	Thickness ($10^{20}\,cm^{-2}$)	Lifetime (h)	Maximum P_3 (±5%) (%)
Astro	11.3	640	1.4	730	58
Pebbles	11.1	508	1.1	350	61
Dino	10.6	452	1.2	700	61
BooBoo	12.6	587	1.4	520	55
Kirk	10.5	624	1.5	600	
Rocky	13.4	773	1.2	100	
Elroy	11.0	430	1.0	100	

The room-temperature lifetimes provide a measure of cell quality because the maximum ^{3}He polarization generally improves with longer lifetimes. The values for P_3 were measured with a monochromatic neutron beam at NIST.

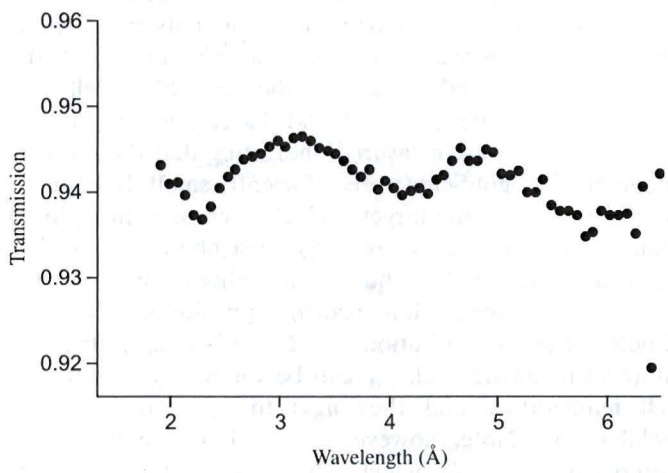

Fig. 2. Transmission of neutrons through a 3.5 mm thick sample of GE-180 glass.

attached to a glass manifold, a rubidium ampoule is placed in a side-arm or a pre-packed glass break-seal ampoule is used. The cell is baked at 400 °C for at least 48 h to a base vacuum below approximately 1×10^{-7} mbar. The cell is then filled with 67 mbar of N_2 followed by about 800 mbar of ^{3}He (99% enrichment) and then sealed at a pull-off with a torch. The filling procedure does not generally make use of LN_2 or LHe cooling of the cell, which is used to produce cells with gas pressures exceeding atmospheric pressure. The cell used for the work described in this paper, BooBoo, is an exception. BooBoo had a short lifetime (55 h) when first filled, and was refilled, after being rinsed in nitric acid, to slightly above atmospheric pressure using LN_2. The polarizations given in Table 1 were produced with a broadband laser system and determined by neutron transmission measurements on the NG6M monochromatic beam line at the NIST Center for Neutron Research [41].

2.4. Cell heating and temperature control

The ^{3}He spin filter cells are mounted in a box made of heat stabilized nylon (MC901 from GE Polymer Shapes). The box is 33 cm wide ×30 cm deep ×26 cm high and maintains the cell at 140–165 °C. The box was designed to be significantly larger than necessary for the cells described in Table 1 in order that larger cells could be used. The neutron beam passes through pairs of 0.2 mm thick, 15 cm diameter single crystal silicon wafers upstream and downstream of the spin-filter cell. A small air gap separates the wafers in each pair. The laser light passes through uncoated glass windows above and below the cell. The oven is heated by hot air that flows through two 750 W in-line air heaters in series. One air heater is located in the shielding cave and provides a constant power. The air heater outside the cave is modulated by a standard PID controller to maintain the selected process temperature. Temperature control to within a few degrees is sufficient. The controlled air heater is placed outside the cave in order to minimize any noise or pick-up of control signals by the detector or data-acquisition system.

2.5. Lasers and optics

Laser light is provided by two fiber-coupled 30 W (nominal) Coherent FAP systems [42]. The FAP systems provide light from a fiber-optic bundle that is coupled to a system of lenses to produce a roughly rectangular "spot" on the cell. The lenses collimate the light so that the rays are nearly parallel, thus mitigating the skew light effect [43]. The unpolarized light from the fiber passes through a polarizing beam splitter which produces two linearly polarized beams, each of which passes through a $\lambda/4$ plate producing two beams with the same circular polarization that overlap at the cell, about 1 m away from the polarizer. One laser beam pair is incident from above, and one is incident from below the cell. The ^{3}He polarization is in the vertical direction and can be parallel or opposite the magnetic field, depending on the orientation of the $\lambda/4$ plates.

The FAP systems were selected as stable robust light sources that could run for months without major adjustment. The laser power and wavelength was occasionally monitored and found to be sufficiently stable for long-term operation, until a laser or power supply failed completely. One particular challenge of the FAP systems is the reduced air cooling effectiveness at 2000 m altitude. The spectral output of the FAP systems is 1.5–2 nm FWHM. This is much greater than the absorption linewidth of rubidium (less than 0.1 nm) though it is less than the p-state splitting. The broadband laser diode arrays (LDAs) are, however, quite effective for rubidium optical pumping, because the rubidium vapor is optically thick, and there is significant absorption even several linewidths off resonance [32]. Polarization over 55% was attained with two broadband, 30 W systems. Narrowed LDA bars have been shown to be more efficient [37,38]. In studies of optical pumping of NPDGamma cells with spectrally narrowed lasers 75% polarization was obtained [7,30]. We expect that in the

future, narrowed LDA bars will be engineered to be sufficiently stable and robust for long-term operation.

2.6. NMR monitoring and polarization reversal

The spin filter was instrumented with pulsed and adiabatic fast passage (AFP) NMR for diagnostics and to reverse the ^{3}He spin. The pulsed NMR used a single small 2.5 cm diameter coil that probed only a small fraction of the cell volume. The coil was placed on the pull-off (a small tube protruding from the side of cell that was used to fill the cell with alkali-metal and gases). The pulsed NMR circuitry switched the coil from the excitation pulse to the read-out electronics. Pulse angles of a few degrees were sufficient for monitoring the polarization. The pulsed NMR was calibrated in a neutron run using the monitors M1 and M2, as described below.

The AFP NMR was used to reverse the ^{3}He polarization with respect to the vertical magnetic field. A set of 30 cm diameter helmoltz coils with their axis along the neutron beam provided the oscillating field. The oscillation frequency was ramped from far below resonance to far above resonance. The losses in AFP reversal depend on the uniformity of the static and oscillating fields and on the sweep parameters: oscillating field strength and sweep rate. With the sweep parameters and field strength empirically tuned to satisfy the adiabatic and fast conditions, losses of much less than 1% (typically 0.1%) were achieved.

2.7. Monitors

Monitors M1 and M2 were used to make a set of measurements from which the neutron and ^{3}He polarizations can be determined. The monitors were 12 cm × 12 cm parallel-plate gas filled ion chambers with two outer high-voltage electrodes and a center collection electrode. The two windows and three electrodes were aluminum alloys. The gas was a mixture of ^{3}He, ^{4}He, and N_2. The ^{3}He thickness was measured to be $(1.01 \pm 0.07) \times 10^{18}\,\mathrm{cm}^{-2}$ for M1 and $(0.99 \pm 0.07) \times 10^{18}\,\mathrm{cm}^{-2}$ for M2 [44]. The expected neutron transmission through the ^{3}He at 5 Å was 94% for each monitor, with additional attenuation and scattering from the aluminum alloy (1 mm of 6061-T6 for each of the two outer windows and 0.5 mm of 3003-H14 for each of the three internal electrodes).

The current from each monitor was converted to a voltage in a preamp, digitized at 62.5 kHZ, and combined into 100 separate 400 μs bins. The preamplifier frequency response was set by a multi-pole filter with 5–7 kHz bandwidth, set to optimize the signal-to-noise ratio for a 400 μs time bin. The data acquisition for each pulse was triggered by a delayed t_0 signal from the proton beam. The charge per pulse for each time bin was collected for a run (typically 10,000 pulses) and the mean, and standard deviation were determined for each time bin. The standard deviation of the distribution was consistent with the expected statistical error estimated from the ^{3}He thickness and the neutron flux incident on each monitor.

The neutron flux at any time is a function of proton current, moderator conditions, guide transmission and neutron wavelength. The signal from M1 was therefore used to normalize the signal measured in M2. The data were acquired synchronously, and thus each time bin corresponded to a different wavelength for M1 and M2. We therefore used M1 as the reference, and interpolated the M2 versus time-of-flight signal to determine $M_2(t_1)$ using the measured distance of 0.4 m between M1 and M2 and allowing the distance from the moderator to M1 to vary as a parameter in the analysis described in Section 3.

In addition to the glass transmission measurement shown in Fig. 2, measurements of the monitor ratios $(M2/M1)$ were made with the following configurations: (1) with the spin filter cell removed but the Si oven windows in place (R_{oven}); (2) with the spin filter cell in place and $P_3 = 0$, i.e. unpolarized ^{3}He (R_0), and (3) with the spin filter cell in place and ^{3}He polarized (R_{P}). Assuming that all backgrounds are accurately subtracted in extracting these ratios, one sees from Eqs. (3) and (4) that, ideally, we expect the following relationships for a uniform thickness of ^{3}He:

$$\frac{R_0(\lambda)}{R_{\mathrm{E}}(\lambda)} = \exp\left(-\sigma_0 t_3 \frac{\lambda}{\lambda_0}\right) \quad \text{and} \quad \frac{R_{\mathrm{P}}(\lambda)}{R_0(\lambda)} = \cosh\left(\sigma_0 t_3 P_3 \frac{\lambda}{\lambda_0}\right). \tag{7}$$

where $R_{\mathrm{E}}(\lambda)$, the monitor ratio that would be measured for an empty cell, is defined in the next section.

3. Results and analysis

In Fig. 3, we show typical raw time-of-flight data, averaged over 10,000 pulses, for M1 and M2 with the ^{3}He spin filter in place. Electronics offsets (pedestals), and beam-off background, including that due to long-lived activation are periodically monitored with beam-off runs measured for the same 40 ms data acquisition window triggered by the proton pulse. The results for several beam-off runs are shown in Fig. 4. These beam-off runs show that the pedestals are typically less than 1% of the signals, but are not constant over the 40 ms acquisition window with variations on the order of a 10^{-3} V, and some evidence of small oscillations. The data for each beam-on run for the M1 and M2 monitors are separately corrected by assuming a constant offset, which is determined by a linear interpolation in time of the offsets determined from two beam-off runs, one before and one after the beam-on run.

Time-of-flight dependent backgrounds include beam related neutrons and short lived activities. Neutrons incident on the monitor detectors during the 40 ms data acquisition window are predominantly the moderated neutrons from the trigger proton pulse, but in principle may also include "wrap around" slow neutrons from earlier pulses, beta-delayed neutrons from fission products

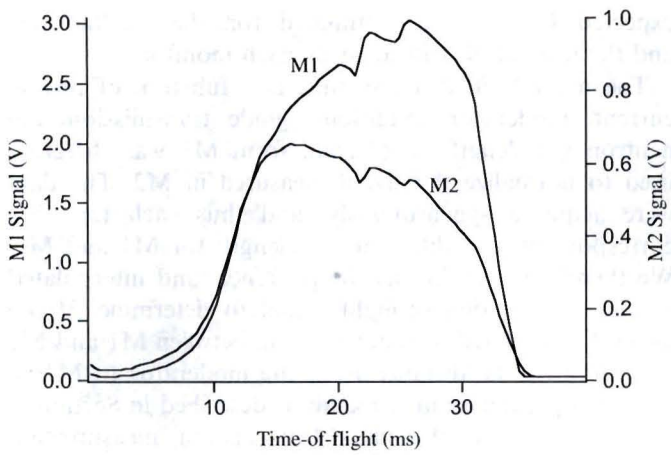

Fig. 3. Raw time-of-flight traces for M1(left axis) and M2 (right axis). The dips near 22 and 26 ms are due to Bragg edges from aluminum windows. The relative deficit in signal at M2 for longer time-of-flight (i.e. longer neutron wavelength) is mostly due to the $1/v$ attenuation in ^{3}He.

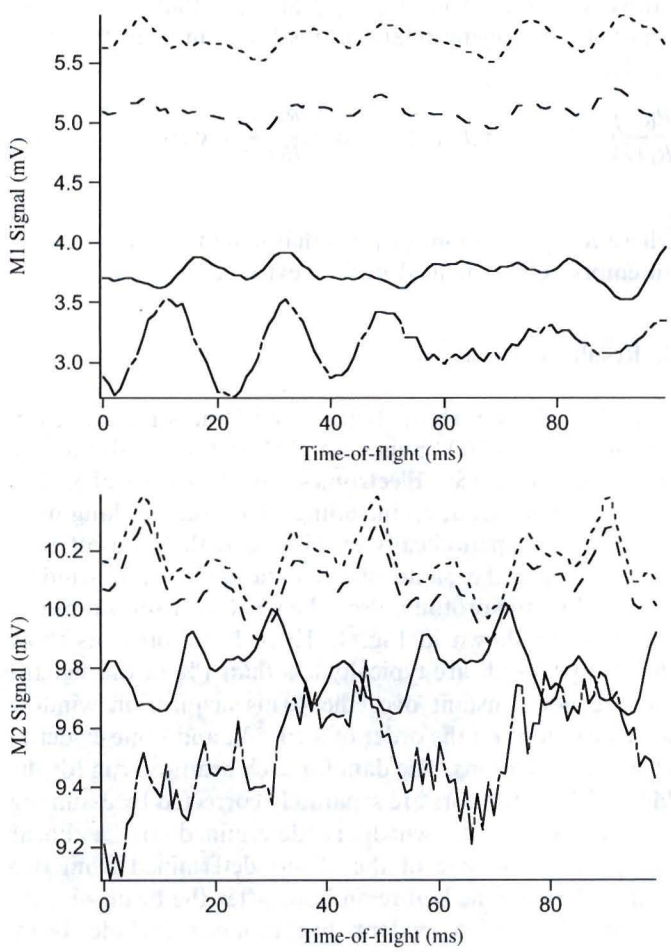

Fig. 4. Beam-off (pedestal) data for M1 and M2. Each trace shows the average of 1000 pulses (50 s). Two traces bracket the February 2005 data (solid and dotted) and two traces are from August 2005 (short dash and long dash). Though the corrections to $M_1(\lambda)$ and $M_2(\lambda)$ are small, the time dependence over the 40 ms data acquisition window and the variation from run-to-run requires interpolation of the correction for each run.

in the tungsten target, and scattered neutrons. Activation could produce gamma-rays, which would be incident on both M1 and M2 with different intensities, but would be compensated in the ratio M_2/M_1 as long as the gamma-ray intensity ratios are constant. Detailed study of these backgrounds will be necessary for precision neutron polarimetry, however for the purposes of this paper, these backgrounds are sufficiently small (i.e. less than a few percent) as discussed below.

Monitor ratios are extracted from background corrected M1 and M2 data. The monitor ratio R_E, which would be measured for an empty spin-filter cell, is given by

$$R_E(\lambda) = R_{oven}[T_{gl}(\lambda)]^{d/3.5} \tag{8}$$

where d is the glass window thickness of the spin-filter cell determined by the best fit of the data, $T_{gl}(\lambda)$ is the glass transmission shown in Fig. 2, and R_{oven} is shown in Fig. 5. The wavelength dependence of R_{oven} is due to the combination of attenuation by the monitors, scattering, collimation and the different wavelength dependence of the monitor efficiencies.

The quantities R_0/R_E and R_P/R_0 as functions of t_1, the time of flight to M1, are fit to the following functional forms derived from Eq. (7):

$$\frac{R_0}{R_{oven}} = A[T_{gl}(\lambda_1)]^{d/3.5}\exp(-\alpha t_1) \quad \text{and}$$
$$\frac{R_P}{R_0} = \cosh(\beta[t_1 - t_0]) \tag{9}$$

where the neutron wavelength at M1 is given by

$$\lambda_1 = \frac{h}{mL_1}t_1 \tag{10}$$

and L_1 is the distance from the moderator to M1 and m is the neutron mass. The parameter t_0 accounts for an offset in the timing with respect to the proton pulse signal.

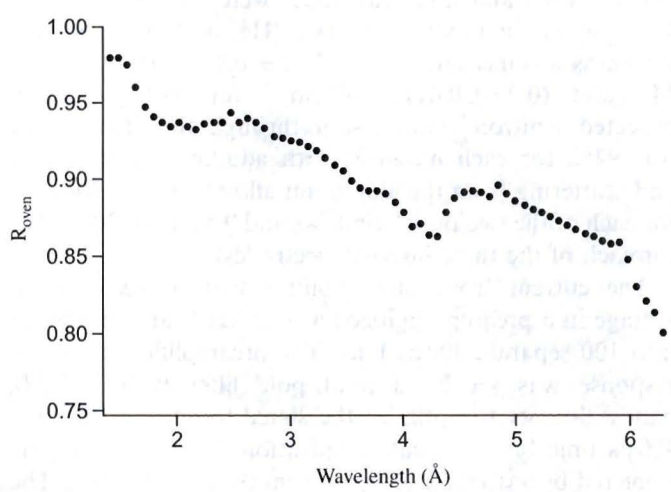

Fig. 5. Monitor ratio R_{oven}, with the cell removed. The wavelength dependence is due to the combination of attenuation by the monitors, scattering, collimation and the different wavelength dependence of the monitor efficiencies. The wavelength is calculated with $L_1 = 20.3$ m.

The free parameters are A, d, α, β, and t_0, with

$$\alpha = \frac{h}{mL_1}\frac{\sigma_0 t_3}{\lambda_0} \quad \text{and} \quad \beta = P_3\alpha. \tag{11}$$

The data, fits, and residuals of the fits are shown in Fig. 6. The best fit cell window thickness is $d = 3.59 \pm 0.12$ mm. The distance from the moderator to M1, L_1, enters the analysis independently (of t_3) only through the interpolation of the M2 data to the time of flight to M1, i.e. precise knowledge of L_1 and t_3 are not necessary. Varying L_1 to minimize χ^2 for the best fit to R_P/R_0 gives the distance to M1 of 20.3 ± 0.8 m, which is consistent with the measured distance (20.73 m) and the Bragg edges observed in a run with a thick piece of beryllium in the beam. The residuals in Fig. 6 indicate wavelength dependent systematic effects of a few tenths of 1%, which is much greater than the statistical error. Potential sources of the systematic effects are discussed in Section 3.1.

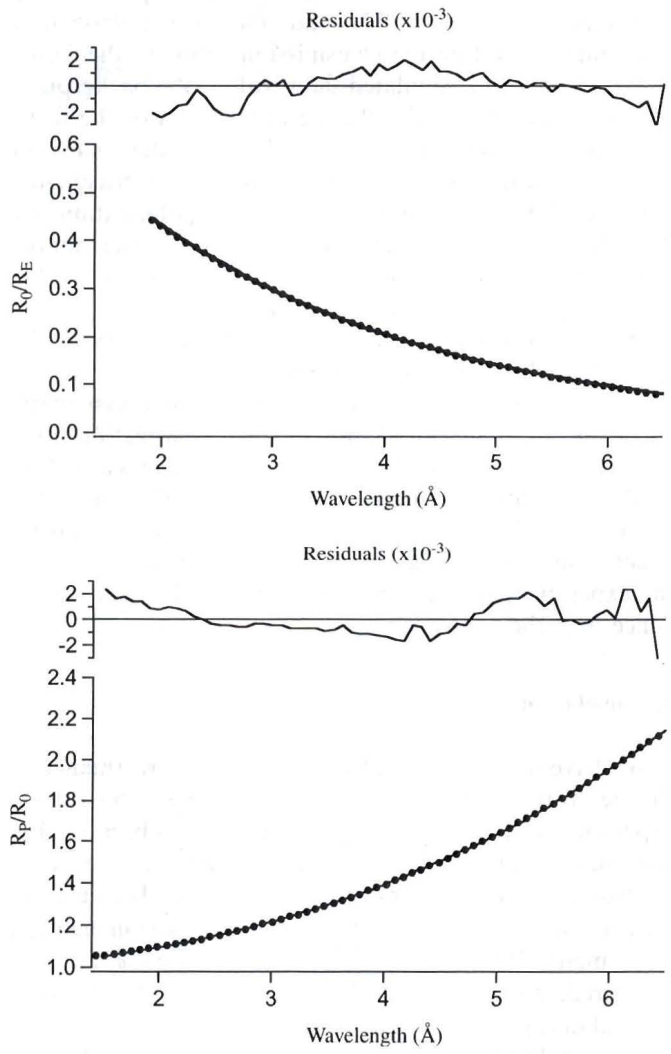

Fig. 6. Results for ratios of monitor ratios. The wavelength is calculated with $L_1 = 20.3$ m. The dots are data and the solid lines are fits to the functions given in Eq. (7). The residuals are shown in the upper portion of each graph.

From Eqs. (3) and (7), the polarization of neutrons emerging from polarized ^{3}He would be given by

$$P(\lambda) = \sqrt{1 - (R_0/R_P)^2}. \tag{12}$$

In Fig. 7, we show $P(\lambda_1)$ for the February 12, 2005, run. The ^{3}He polarization and t_3 can also be derived from this analysis. For the February 12, 2005, run, we find $P_3 = 57 \pm 1\%$. The uncertainty is discussed in Section 3.1.

The ^{3}He polarization as a function of time after January 1, 2005, is shown in Fig. 8. There are several notable features to Fig. 8. First, the time constant for the ^{3}He polarization, after it is destroyed, is many hours, typical of spin-exchange optical pumping. Note also that the steady-state ^{3}He polarization appears to be slowly but steadily decreasing throughout 2005. We have considered several possible sources of this decrease in maximum attainable ^{3}He polarization: cell degradation, changing magnetic field

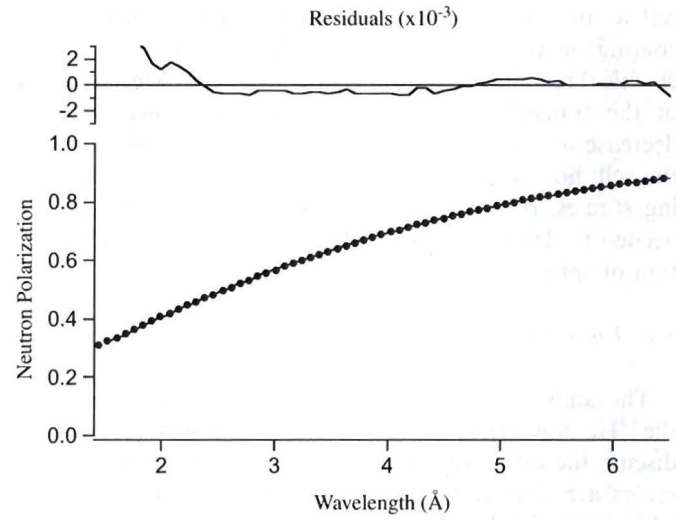

Fig. 7. Neutron polarization as defined in Eq. (12) as a function of neutron wavelength calculated with $L_1 = 20.3$ m. The dots are data and the solid line is a fit to the form of Eq. (3), with the residuals shown in the upper panel.

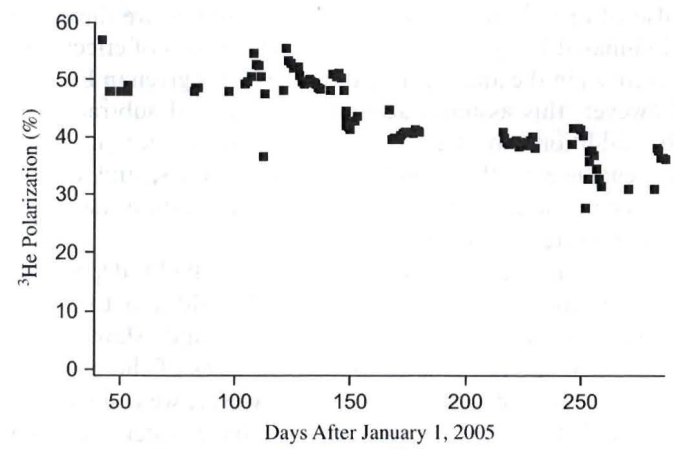

Fig. 8. Estimated ^{3}He polarization measured with neutron transmission throughout the 2005 run.

environment, laser drift and optical alignment changes. Cell degradation could affect the ^{3}He polarization relaxation time, the density and/or polarization of the rubidium at a given temperature, and the coupling or transmission of laser light into the cell. The ^{3}He relaxation depends on the ^{3}He density [33], the cell walls, contaminants—in particular O_2, magnetic field gradients, and possible Rb density or temperature dependence. Near the end of the run, the ^{3}He relaxation time was measured with the NMR and found to be greater than 150 h, consistent with earlier measurements. The rubidium polarization in the cell is position dependent and depends on the laser intensity, the cell walls, the composition of gases and contaminants in the cell volume. In previous experiments with spin-exchange polarized ^{3}He targets and neutron spin filters [45,46], the cells and polarization have proved quite stable provided the cell temperature and laser characteristics were stable; however, there is no prior experience with GE-180 cells pumped at high temperatures for 1.5 years. Visual examination of the cell at the end of the 2005 run revealed a milky white coating on the inside surface of the cell, possibly due to chemical reaction of the rubidium and glass. Measurement of the transmission of 795 nm light confirmed a sharp decrease in the laser power getting to the rubidium inside the cell; however, further diagnostics, systematic engineering studies, or experience with several more cells will be needed to definitively understand any systematic degradation of spin filter cells.

3.1. Uncertainty estimates

The analysis presented above provides information on the ^{3}He thickness and polarization. In this section, we discuss the estimated uncertainties. Statistical and related errors are ultimately limited by neutron statistics and by white noise in the electronics (Johnson noise, etc.). With 10^7 neutrons per pulse, neutron counting statistics determine the statistical error. For 10,000 pulses and a few percent monitor efficiency, the relative statistical error should be less than 10^{-4} for a 500 s run. The oscillations apparent in some of the beam-off runs shown in Fig. 4 are also of order a few $\times 10^{-4}$. The uncertainties are therefore dominated by systematic effects. A large class of effects are removed in the analysis based on the ratios given in Eq. (7); however, this assumes accurate background subtractions. In addition to backgrounds, non-linearities or rate dependence in the monitors and electronics, and uncertainty in the neutron wavelength determination may give rise to systematic effects.

There are several sources of time-of-flight dependent backgrounds in both M1 and M2. In addition to wrap-around neutrons, scattered neutrons and short lived activation should be considered. The sizes of these effects have not been directly measured; however, we can explore their effects through simulations. We have undertaken two kinds of simulations: (1) simulation of the M2 signal based on a model of the spin filter and windows with added backgrounds and (2) simulated corrections to M_1 and M_2 with a generic background linear in time of flight.

The simulated M2 signal ($M_2'(\lambda)$) was generated from the M1 signal:

$$M_2'(\lambda) = \left[\alpha R_E(\lambda) M_1(\lambda) e^{-\sigma_0 t_3(\lambda/\lambda_0)} \cosh\left(\sigma_0 t_3 P_3 \frac{\lambda}{\lambda_0}\right)\right] + (A\lambda + B) \quad (13)$$

where α is the wavelength independent attenuation, and A and B are coefficients that represent a linear background *difference* for M1 and M2. This background model, for M_1 or M_2, is generic and could approximate any of the considered effects, i.e. scattered neutrons, background gammas, activation, wrap-around neutrons, and non-linearities. The simulated data are then analyzed as usual. Results for $A = 0.002\,\mathrm{V/Å}$ and $B = -0.01\,\mathrm{V}$ are shown in Fig. 9. The residuals are similar in shape to those apparent in Fig. 6. In general, backgrounds less than a few percent are possible without affecting $M_1(\lambda)$ and $M_2(\lambda)$ unreasonably. These effects in turn change the neutron polarization determined from Eq. (12) and the ^{3}He polarization determined by fitting the transmission ratios to the forms of Eq. (7). For the simulated data with 3–5% background added to M1 or M2, the change in residuals of the fit to neutron polarization at 5 Å is $\approx 0.1\%$, and the change in ^{3}He polarization is $\approx 1\%$. This provides a reasonable estimate of the uncertainty on the ^{3}He polarization for these low-background data, and emphasizes the importance of low and well understood backgrounds for attaining precision neutron polarimetry.

Due to the nature of blown glass, the windows of the spin filter cell are not perfectly flat or parallel. Numerical study of the effects of curved windows shows a systematic correction of about +0.1% for the ^{3}He polarization for a 10 cm diameter cell that is 5 cm thick at the edges and 7 cm in the in center. With non-uniform ^{3}He thickness, the neutron polarization, given by Eq. (3), is also non-uniform, which could lead to systematic effects that depend on how the experiment or measurement averages the spin dependence over the neutron beam area.

4. Conclusion

We have described the construction and performance of the neutron spin filter developed for the $\vec{n} + p \rightarrow d + \gamma$ experiment at Los Alamos. The spin filter has been used in test and commissioning runs to polarize a large area neutron beam, and a pair of thin monitors has been used to measure the polarization and evaluate precision neutron polarimetry. Polarization of ^{3}He as high as 57% has been measured, but the ^{3}He polarization is not stable and a general decay was observed over 1 year of operation, with average polarization of 43%. The exact reasons for the unstable and decaying ^{3}He polarization are not determined, but may be related to increased optical opacity of the glass cell.

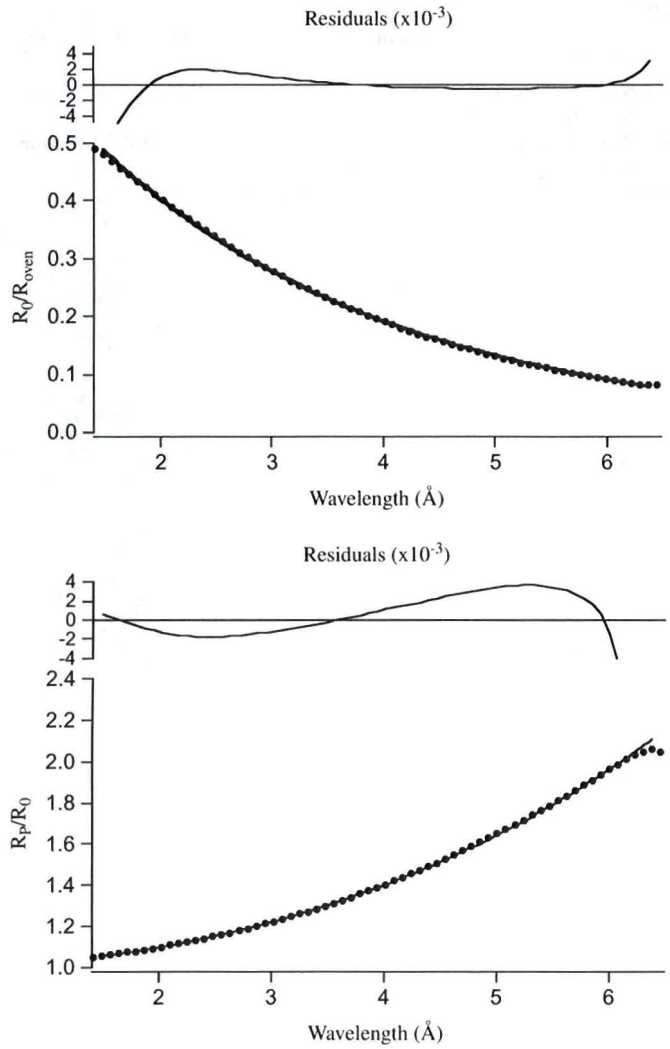

Fig. 9. Results for simulated data with background added to the signal from M1 as described in the text.

The beam transmission monitors have been used to determine the neutron polarization, averaged over the neutron beam, with high accuracy. The uncertainty is estimated to be $\approx 0.1\%$ at 5 Å. The wavelength dependence of the transmission ratios show residuals at the level of 0.1% of the transmission ratios. These residuals may be due to backgrounds, activation, or non-linearities. Simulations show that these could be due to a simple form of background or distortion and suggest that significant improvement below 0.1% neutron polarization precision will be possible with greater control of backgrounds.

Improvements to the spin filter will require a full understanding of the unstable and decaying polarization. The available laser power will be increased, and the cell replaced. In the long term, narrowed laser diode array bars may improve polarization and long-term performance. A number of other intriguing changes are under consideration, including spin-filter cells with hybrid-alkali mixtures, for example rubidium and potassium [47].

Acknowledgments

The authors wish to express gratitude to the entire $\vec{n} + p \rightarrow d + \gamma$ collaboration for its efforts related to the experiment and the work described in this paper. This work was supported by the US National Science Foundation, the Department of Energy, and NIST.

References

[1] W. Heil, K. Andersen, D. Hoffman, H. Humbolt, J. Kulda, E. Lelievre-Berna, O. Schärpf, F. Tasset, Physica B 241 (1998).
[2] L. Lising, et al., Phys. Rev. C 62 (2000) 055501.
[3] D.A. Smith, et al., Phys. Rev. C 65 (2002) 035503.
[4] H. Abele, et al., Phys. Rev. Lett. 88 (2002) 211801.
[5] P.R. Huffman, et al., J. Res. Natl. Inst. Stand. Technol. 110 (2005) 299.
[6] T.E. Chupp, K.P. Coulter, Phys. Rev. Lett. 55 (1985) 1074.
[7] T.R. Gentile, W.C. Chen, G.L. Jones, E. Babcock, T.G. Walker, J. Res. Natl. Inst. Stand. Technol. 110 (2005) 299.
[8] K.H. Andersen, et al., Physica B 356 (2005) 103.
[9] W.M. Snow, J. Res. Natl. Inst. Stand. Technol. 110 (2005) 189.
[10] T. Soldner, et al., Phys. Lett. B 581 (2004) 49.
[11] W.S. Wilburn, et al., J. Res. Nat. Inst. Stand. Technol. 110 (2005) 389.
[12] T.E. Chupp (spokesman) et al., Letter of Intent to SNS Fundamental Neutron Physics Beam Program Advisory Committee, Oak Ridge National Lab, 2005.
[13] G.S. Mitchel, et al., Nucl. Instr. and Meth. A 521 (2004) 468.
[14] P.-N. Seo, et al., Nucl. Instr. and Meth. A 517 (2004) 285.
[15] P.-N. Seo, et al., J. Res. Natl. Stand. Technol. 110 (2005) 145.
[16] M.T. Gericke, et al., Nucl. Instr. and Meth. A 540 (2005) 328.
[17] W.S. Wilburn, J.D. Bowman, S.I. Penttila, M.T. Gericke, Nucl. Instr. and Meth. A 540 (2005) 180.
[18] K.P. Coulter, et al., Nucl. Instr. and Meth. A 270 (1988) 90.
[19] S.F. Mughabghab, M. Divadeenam, N.E. Holden, Neutron resonance parameters and thermal neutron cross sections, Neutron Cross Sections, vol. 1, Academic Press, New York, 1981.
[20] M.A. Bouchiat, T.R. Carver, C. Varnum, Phys. Rev. Lett. 5 (1960) 373.
[21] T.E. Chupp, R.A. Loveman, A.K. Thompson, A.M. Bernstein, D.R. Tierger, Phys. Rev. C 45 (1987) 915.
[22] K.P. Coulter, et al., Nucl. Instr. and Meth. A 288 (1989) 463.
[23] D.R. Rich, et al., Nucl. Instr. and Meth. A 481 (2002) 431.
[24] J.R. Johnson, et al., Nucl. Instr. and Meth. A 356 (1995) 148.
[25] W. Xu, et al., Phys. Rev. Lett. 85 (2000) 2900.
[26] X. Zheng, et al., Phys. Rev. C 70 (2004) 065207.
[27] T.E. Chupp, S.D. Swanson, Adv. A Mol. Opt. Phys. 43 (2000) 42.
[28] M.E. Wagshul, T.E. Chupp, Phys. Rev. A 44 (1994) 3854.
[29] S. Appelt, A. Ben-Amar Baranga, C.J. Erickson, M.V. Romalis, A.R. Young, W. Happer, Phys. Rev. 58 (1998) 1412.
[30] E. Babcock, et al., Phys. Rev. Lett. 96 (2006) 083003.
[31] T.G. Walker, W. Happer, Rev. Mod. Phys. 69 (1997) 629.
[32] M.E. Wagshul, T.E. Chupp, Phys. Rev. A 24 (1989) 4447.
[33] N.R. Newbury, A.S. Barton, G.D. Cates, W. Happer, H. Middleton, Phys. Rev. A 48 (1993) 4411.
[34] L.D. Schearer, G.K. Walters, Phys. Rev. 139 (1965) A1398.
[35] E.M. Purcell, Phys. Rev. 117 (1960).
[36] T.B. Smith, et al., Nucl. Instr. and Meth. A 402 (1997) 247.
[37] B. Chann, et al., J. App. Phys. 94 (2003) 6908.
[38] J.N. Zerger, et al., Apl. Phys. Lett. 76 (2000) 1798.
[39] GE Lighting Component Sales, Bldg. 315D, 1975 Noble Rd., Cleveland, OH 44117. Certain trade names and company products are mentioned in the text or identified in an illustration in order to adequately specify the experimental procedure and equipment used.

In no case does such identification imply recommendation or endorsement by the authors' institutions, nor does it imply that the products are necessarily the best available for the purpose.
[40] D.R. Rich, T.R. Gentile, T.B. Smith, A.K. Thompson, G.L. Jones, Appl. Phys. Lett. 80 (2002) 2210.
[41] G.L. Jones, et al., Nucl. Instr. and Meth. A 440 (2000) 772.
[42] Coherent Corporation FAP System. See Ref. [38] for disclaimer.
[43] B. Chann, et al., Phys. Rev. A 66 (2002) 033406.
[44] R.C. Gillis, 3He ionization chambers as neutron beam monitors for the NPDGamma experiment, M.Sc. Thesis, University of Manitoba, CA, 2006, Unpublished.
[45] K.P. Coulter, A.B. McDonald, G.D. Cates, W. Happer, T.E. Chupp, Nucl. Instr. and Meth. A 276 (1989) 29.
[46] W.J. Cummings, O. Häusser, W. Lorenzon, D.R. Swenson, B. Larson, Phys. Rev. A 51 (1995) 4842.
[47] E. Babcock, et al., Phys. Rev. Lett. 91 (2003) 123003.